ACS OMEGA

http://pubs.acs.org/journal/acsodf

Article

Incorporation of Cesium Lead Halide Perovskites into g-C_3N_4 for Photocatalytic CO_2 Reduction

Ruolin Cheng, Handong Jin, Maarten B. J. Roeffaers, Johan Hofkens,* and Elke Debroye*

Cite This: *ACS Omega* 2020, 5, 24495−24503

Read Online

ACCESS | Metrics & More | Article Recommendations | Supporting Information

ABSTRACT: $CsPbBr_3$ perovskite-based composites so far have been synthesized by postdeposition of $CsPbBr_3$ on a parent material. However, *in situ* construction offers enhanced surface contact, better activity, and improved stability. Instead of applying a typical thermal condensation at highly elevated temperatures, we report for the first time $CsPb(Br_xCl_{1-x})_3$/graphitic-C_3N_4 ($CsPbX_3$/g-C_3N_4) composites synthesized by a simple and mild solvothermal route, with enhanced efficacy in visible-light-driven photocatalytic CO_2 reduction. The composite exhibited a CO production rate of 28.5 μmol g^{-1} h^{-1} at an optimized loading amount of g-C_3N_4. This rate is about five times those of pure g-C_3N_4 and $CsPbBr_3$. This work reports a new *in situ* approach for constructing perovskite-based heterostructure photocatalysts with enhanced light-harvesting ability and improved solar energy conversion efficiency.

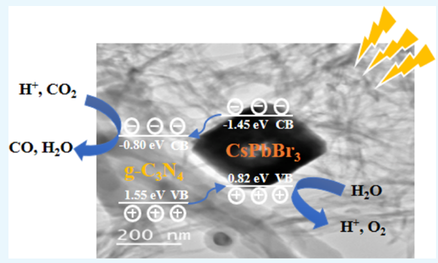

1. INTRODUCTION

The increasing emission of greenhouse carbon dioxide (CO_2) and the imminent shortage of energy supplies have drawn extensive public attention. Thanks to the pioneering work on TiO_2 in water splitting,[1] artificial photosynthesis has become one of the most promising methods to convert solar energy to chemical resources such as CO, CH_4, and CH_3OH.[2] It is generally known that CO_2 is a stable linear molecule and its unreactive nature requires very high energy or strong reductive agents to initiate its reduction reaction. Moreover, the single-electron reduction of CO_2 to the anion radical $CO_2^{\bullet-}$ has a strong negative electrochemical potential of −1.9 V *versus* the normal hydrogen electrode (NHE).[3] To circumvent this problem, Tran *et al.* reported that proton-assisted transfer of multiple electrons enables straightforward CO_2 photoreduction.[4] So far, a substantial number of materials and their composites have been reported to function as electrocatalysts and/or photocatalysts for CO_2 reduction.[5] However, the search for new photocatalytic materials with improved performance is still ongoing.

Recently, halide perovskites with an ABX_3 structure [A = $CH_3NH_3^+$ (MA), $HC(NH_2)_2^+$ (FA), Cs^+; B = Pb^{2+}, and Sn^{2+}; X = I^-, Br^-, and Cl^-] have emerged as an excellent class of light absorbers for the use in solar cells.[6] These materials have attracted attention around the globe for their excellent properties: cheap and easy fabrication process, tunable small band gaps, high absorption coefficients, and extremely long-range balanced electron and hole transport lengths.[6,7] What is more, owing to the energy level of the conduction band (CB), they have a good reduction ability to achieve H_2 generation and CO_2 reduction.[8] However, halide perovskites are not stable in a polar environment, and reactions are conventionally performed in nonpolar or relatively low polarity solvents. Fortunately, all-inorganic perovskites, especially cesium lead halide ($CsPbX_3$, X = Cl, Br, and I), offer an improved stability and nonhygroscopicity.[9,10] As a prominent representative, cesium lead bromide ($CsPbBr_3$) has been seen as a potential candidate for photocatalysis, especially for photocatalytic CO_2 reduction.[11−14]

Several strategies have been employed to further improve the activity and stability of halide perovskites in polar solvents. First, $CsPbX_3$ is coupled with other photocatalysts, including TiO_2,[15] g-C_3N_4,[16] MXene,[17] and UiO-66-NH_2.[18] Secondly, it can be encapsulated in porous materials such as metal−organic frameworks (MOFs, ZIF-8,[19] and ZIF-67[20]) or core−shell structure, which helps in maintaining its structural stability and photoactivity. Solar cell-like architectures have been explored to prevent direct contact of perovskites with polar solvents, providing another effective route toward long-term stabilization.[21,22] The anion exchange approach is also widely investigated to tune the optical and structural properties of $CsPbX_3$.[23−25]

Herein, we construct a novel $CsPbX_3$/g-C_3N_4 composite by *in situ* polymerization for the first time. Graphitic carbon nitride (g-C_3N_4) with a graphene-like two-dimensional structure, high physicochemical stability, and a medium band gap (2.7 eV) has been introduced as a promising candidate for visible light photocatalytic conversion of CO_2 and is widely

Received: June 19, 2020
Accepted: August 11, 2020
Published: September 16, 2020

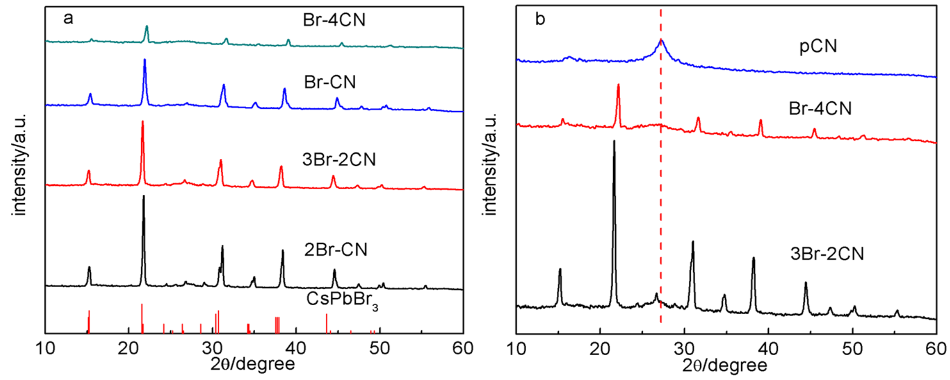

Figure 1. XRD patterns of (a) all the synthesized $CsPbX_3/g\text{-}C_3N_4$ composites and (b) pCN, 3Br−2CN and Br−4CN.

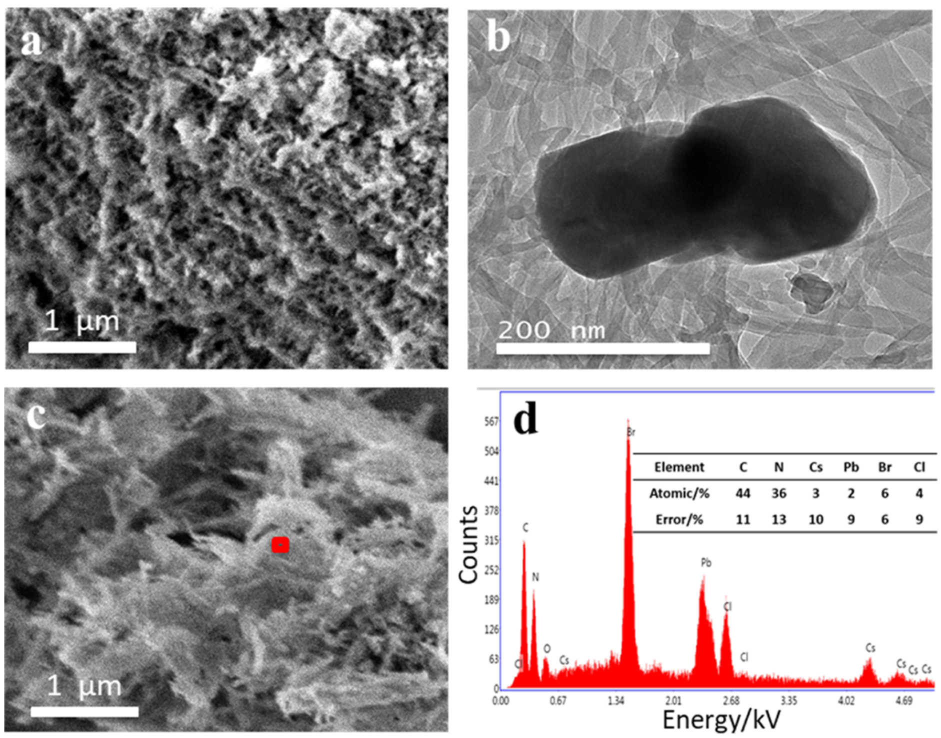

Figure 2. (a) Typical SEM image of pCN, (b) TEM, and (c) SEM images of 3Br−2CN; (d) EDS result of the selected region in (c).

used to hybridize with other photocatalysts.[26−28] Compared to the postsynthesis self-assembly of the composite,[27] *in situ* construction could offer enhanced surface contact, better activity, and improved stability.[29] Different from the typical thermal condensation at 550 °C to synthesize $g\text{-}C_3N_4$, solution synthesis is a mild route suitable for *in situ* perovskite-based composite construction.[30] In this approach, acetonitrile is used as the solvent instead of water or other polar solvents, to minimize perovskite degradation.

2. RESULTS AND DISCUSSION

A series of $CsPbX_3/g\text{-}C_3N_4$ composites with varying composition have been synthesized by *in situ* growth, as described in the Experimental Section. X-ray diffraction (XRD) measurements were performed to reveal the crystal structure of the parent components ($CsPbBr_3$ and $g\text{-}C_3N_4$) and all composites. Starting with orthorhombic $CsPbBr_3$ (Figure S1a), the composites maintain the original perovskite crystal structure. With increasing amounts of $g\text{-}C_3N_4$ introduced into the system, the peaks corresponding to the (100), (110), (111), (200), (211), and (202) diffractions of $CsPbBr_3$ monotonically shift toward higher angles because of the lattice contraction caused by Br-to-Cl anion exchange during the synthesis.[31] Simultaneously, the (002) peak of $g\text{-}C_3N_4$ at 27.4° becomes dominant, while the diffraction peaks of $CsPbBr_3$ get weaker (Figure 1b).

The morphology and elemental composition of the as-synthesized samples were characterized by scanning electron microscopy (SEM) and transmission electron microscopy (TEM). pCN is composed of a network of nanobelts (Figure 2a), and pure $CsPbBr_3$ has a uniform cubic shape (Figure S2). In the further discussion on characterization, especially the 3Br−2CN composite is focused on because it exhibited the best photocatalytic performance, as will be discussed at the end of this section. 3Br−2CN mainly exhibits the same morphology as pCN (Figures 2b and S2a); nevertheless, energy-dispersive spectrometry (EDS) elemental analysis of a selected region confirms the coexistence of both $CsPbX_3$ and $g\text{-}C_3N_4$ (Figure 2c). Moreover, TEM imaging and element

https://dx.doi.org/10.1021/acsomega.0c02960
ACS Omega 2020, 5, 24495−24503

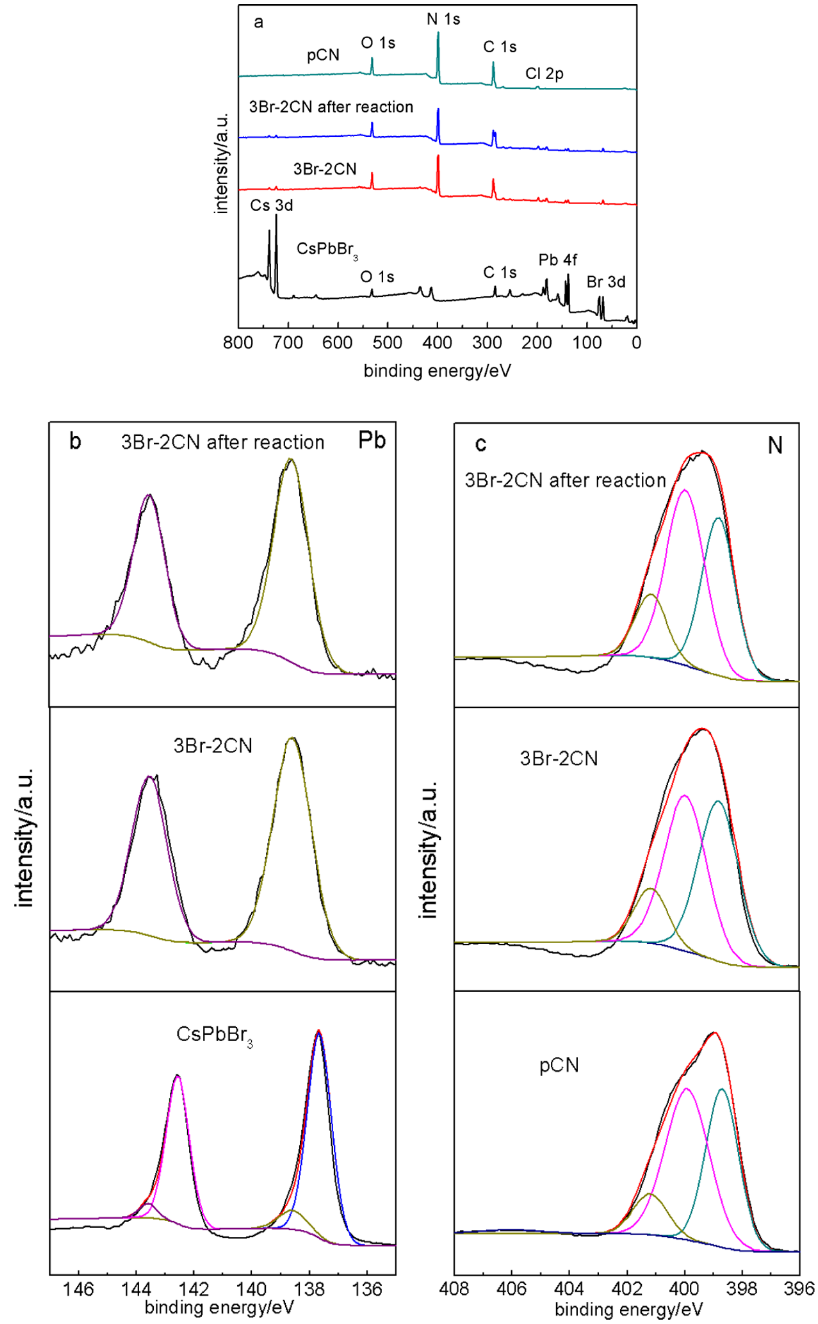

Figure 3. XPS spectra of $CsPbBr_3$ and 3Br−2CN (a) survey, (b) Pb 4f, and (c) N 1s.

mapping of 3Br−2CN (Figures 2b and S3) support the *in situ* growth of $g\text{-}C_3N_4$ on $CsPbBr_3$, encapsulating the perovskite.

Thermal stability and sample composition were investigated by thermogravimetric analysis (TGA) (Figure S4). pCN has two weight loss regions: the first one is when heating from room temperature to 100 °C, which is due to the adsorbed H_2O; the second one is from 350 to 500 °C. Above 500 °C, pCN is fully decomposed, and hardly any substance remains.[32] Pure $CsPbBr_3$ (onset *ca.* 600 °C) is more thermally stable than pure $g\text{-}C_3N_4$.[33] Hence, the rapid weight decrease of the composites in the temperature range of 350−550 °C could be assigned to the decomposition of $g\text{-}C_3N_4$. Notably, the composites possess higher decomposition temperatures than that of pCN, which reveals the higher thermal stability of the composites.

The surface chemical composition and chemical states of the as-synthesized composites were revealed by an X-ray photoelectron spectroscopy (XPS) survey spectrum and relative high-resolution spectra. 3Br−2CN shows distinct signals belonging to C, N, O, Cl, Cs, Pb, and Br, suggesting the successful synthesis of the $CsPbX_3/g\text{-}C_3N_4$ composite (Figure 3a). Notably, the composite demonstrates a decreased intensity of Cs 3d, Pb 4f, and Br 3d peaks compared to the pure $CsPbBr_3$, suggesting that the $CsPbBr_3$ particles were encapsulated by $g\text{-}C_3N_4$.[3434]

Four distinct chemical states of carbon are identified (Figure S5b). Typically, the peak centered at 284.8 comes from sp^2 C−C bonds, while the peaks at 286.3 and 288.6 eV are ascribed to C−N bonds in carbon species and sp^2 bonded carbon (N−C═N) in the triazine rings, respectively.[35] The peak at 290 eV

https://dx.doi.org/10.1021/acsomega.0c02960
ACS Omega 2020, 5, 24495−24503

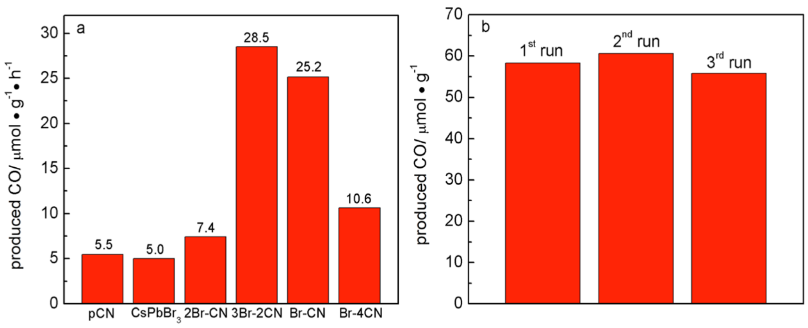

Figure 4. Photocatalytic CO_2 reduction on (a) pCN, $CsPbBr_3$, and $CsPbX_3$/g-C_3N_4 composites under visible light irradiation $\lambda > 420$ nm; (b) stability test of CO_2 photoreduction on 3Br−2CN for three consecutive runs of 2 h each.

Table 1. Physical Parameters of the Prepared $CsPbX_3$/g-C_3N_4 Catalysts

sample	pCN	$CsPbBr_3$	2Br−CN	3Br−2CN	Br−CN	Br−4CN
S_{BET}/m^2 g^{-1}	45	0.2	21	68	54	47
bandgap/eV	2.35	2.27	2.42	2.46	2.47	2.38

is ascribed to deposited carbon. As can be seen in Figure 3c, in the N 1s spectra of pCN can be fitted according to traditional g-C_3N_4.[36] The dominating peak at 398.6 eV is from the sp^2 nitrogen (C═N−C). The peak belonging to the tertiary nitrogen bonded to carbon atoms in the form of N−(C)3 is at 399.9 eV and the one at 401.2 eV originates from amino functional groups (C−N−H). The same patterns of C 1s and N 1s spectra can be found in 3Br−2CN, confirming the successful formation of the composite.

Cs 3d peaks observed in the range of 720−745 eV shift to higher binding energy in the composite (Figure S5a). This phenomenon has also been found in other $CsPbBr_3$ composites.[37] The Pb 4f spectra (Figure 3b) of pure $CsPbBr_3$ show two main peaks of metallic Pb at 137.6 and 142.5 eV, corresponding to the $4f_{7/2}$ and $4f_{5/2}$, respectively. The peaks of the Pb^{2+} state with a nearly identical coordination environment only occupy a small surface area at 138.6 and 143.8 eV, which might be the result of beam damage during the measurement.[38] On the contrary, 3Br−2CN exhibits peaks attributed to the Pb^{2+} oxidation state.

Br 3d has two sets of binding energies, one at 67.6 eV for core species and another one at 68.6 eV for surface ions (Figure S5c).[39] The contribution of Br species at 68.6 eV in the composite increased, suggesting this species to be more dominant on its surface. The Cl $2p_{3/2}$ spectra can be deconvoluted into two sub-bands. The one at 200 eV can be attributed to the C−Cl functionalities in the sample, while the one at 197.4 eV indicates the presence of ionic chloride (Figure S5d).[40] Each set of $2p_{1/2}$ and $2p_{3/2}$ peaks is separated by a spin−orbit splitting of 1.6 eV.[41]

The photoreduction activities of the obtained $CsPbX_3$/g-C_3N_4 composites, pure $CsPbBr_3$, and pCN are presented in Figures 4a and S7. Control experiments to confirm the observed CO_2 reduction were performed first. In the absence of light irradiation or CO_2 (under He atmosphere) or without any photocatalyst added, no appreciable CO or other kinds of hydrocarbons were detected. In the real experiment under visible light irradiation (420−800 nm), both pure $CsPbBr_3$ and pCN show a similar CO production rate of about 5 μmol g^{-1} h^{-1}. The composite materials exhibit an enhanced photocatalytic activity, of which 3Br−2CN shows the best photoreduction performance with a CO production rate of 28.5 μmol g^{-1} h^{-1}, which is about 5.7 times that of pure $CsPbBr_3$ and 5.2 times higher than pCN. To evaluate the effect of water, a test experiment in high purity CO_2 gas without H_2O was performed. The CO amount generated after 4 h reduced by 80%, confirming the critical role of water in this photoreduction process.

For comparison, g-C_3N_4 (CN) synthesized by the traditional calcination of urea and commercial anatase TiO_2 were used as reference photocatalysts. Under visible light irradiation, the formation rate of CO over g-C_3N_4 is 4.9 μmol g^{-1} h^{-1}, in comparison to 7.1 μmol g^{-1} h^{-1} in literature.[42] Without the 420 nm cut-off filter, anatase TiO_2 has a CH_4 formation rate of 4.3 μmol g^{-1} h^{-1}, which is similar to the 5.9 μmol g^{-1} h^{-1} reported.[43] As an additional test, we applied the precipitation method as reported in the literature[44] to synthesize the $CsPbX_3$/g-C_3N_4 composite with a 1:1 weight ratio of $CsPbBr_3$ to g-C_3N_4. This composite sample has a CO formation rate of 15.2 μmol g^{-1} h^{-1}, which is nearly half of the CO production rate obtained via the newly introduced solution-based route.

To evaluate the stability of the composites, three consecutive runs of 2 h each were performed on 3Br−2CN (Figure 4b). Only 4% activity loss was found after 6 h. Six consecutive recycling photocatalytic tests of 4 h each (in total 24 h) (Figure S8b) were further conducted on 3Br−2CN. The CO production decreased by 17% after three cycles and 50% after six cycles. To understand the stability of the composite, XRD was used. For pure $CsPbBr_3$, diffraction peaks of $CsPb_2Br_5$ could be observed after 4 h reaction, resulting from the degradation of $CsPbBr_3$ (shown in Figure S1b). For 3Br−2CN (shown in Figure S1c), the crystal structure was well conserved after three runs (in total 12 h); however, the decreased CO formation rate could be contributed to a gradual deactivation of the catalyst.[45,46] After six runs, diffraction peaks of $CsPb_2Br_5$ appeared, explaining the substantially reduced performance.[47] XPS measurements were also performed on 3Br−2CN after six runs, but no significant difference in the XPS survey and high-resolution spectra was observed (Figures 3 and S5). For comparison, the stability test was also performed in an acetonitrile/water system according to the literature.[27] The composite remained stable after 6 h (Figure S8a).

To reveal the photocatalytic mechanism of the $CsPbX_3$/g-C_3N_4 composite, the compound surface area, the energy level

https://dx.doi.org/10.1021/acsomega.0c02960
ACS Omega 2020, 5, 24495−24503

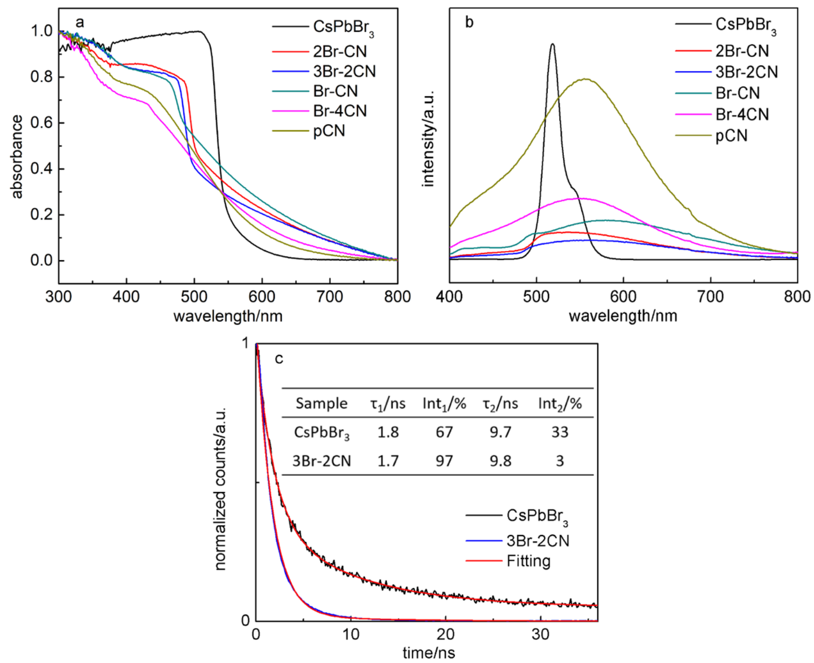

Figure 5. (a) UV−vis DRS of the as-prepared samples, (b) PL spectra at an excitation wavelength of 380 nm, (c) time-resolved PL decay signal of pure $CsPbBr_3$ and 3Br−2CN fitted with biexponential decay kinetics, including the corresponding fitting parameters.

of photoinduced electrons, band gap, and separation efficiency of charge carriers need to be investigated.

The specific surface areas studied by N_2 adsorption−desorption measurements (Figure S9), together with the band gap data (Figure S10a) of as-obtained samples, are listed in Table 1. From the measured surface areas, the pure $CsPbBr_3$ seems to be relatively compact. The introduction of g-C_3N_4 greatly increases the catalysts' specific surface area. Among all the composite samples, 3Br−2CN possesses the highest specific surface area of 68 m^2 g^{-1}, which favors the exposure of active sites, promotes the adsorption of CO_2 molecules, and consequently improves catalytic performance.

Normalized UV−vis diffuse reflectance spectra (DRS) of the $CsPbX_3$/g-C_3N_4 photocatalysts, shown in Figure 5a, were recorded to reveal the light-harvesting ability. All samples have UV and visible light response. Compared to pure $CsPbBr_3$, the composites show an obvious increase of absorption above 550 nm because of the introduction of g-C_3N_4. Meanwhile, the absorption edge of the $CsPbBr_3$ fraction shifts from about 525 nm to the lower wavelength in the composites. This blue shift is due to the Br-to-Cl anion exchange, which is also visible in the XRD patterns.[24,31]

Photoluminescence (PL) spectra were recorded applying a 380 nm excitation. When compared to the thermal condensation way to synthesize g-C_3N_4, this solvothermal processing could improve the p-electron delocalization in the conjugated system, thus modifying the intrinsic optical property of pCN. Shown in Figure 5b, pCN has a broad peak centered at ∼560 nm, which is ascribed to the intrinsic lowest unoccupied molecular orbital to highest occupied molecular orbital emission of g-C_3N_4, corresponding to its band gap. $CsPbBr_3$ has a peak centered at ∼520 nm. The peak pattern of both $CsPbBr_3$ and pCN can be found in all composites. According to the literature, the Br to Cl anion-exchange would cause the gradual PL peak shift to higher energies.[39,48] The typical PL peaks of $CsPbBr_3$, $CsPbCl_3$ and $CsPbClBr_2$ are positioned at 520, 457,[49] and 471 nm,[50] respectively. Thus, the ratio of Br to Cl in the composites is above 2:1.[51] Clearly, PL intensity of the composites exhibits a significant decrease. Among all the composites, 3Br−2CN has the lowest intensity, indicating the effectively suppressed radiative recombination of charge carriers inside the composite system. This is beneficial because the electrons are then more available for carrying out the photocatalytic reduction.

Time-resolved PL decay curves of $CsPbBr_3$ and the composite 3Br−2CN were measured and fitted with a biexponential decay function (Figure 5c). The short and long PL lifetimes can be assigned to radiative and non-radiative recombination, respectively.[15] The average lifetime was calculated by the following equation: $\tau_{avg} = (A_1\tau_1^2 + A_2\tau_2^2)/(A_1\tau_1 + A_2\tau_2)$ and showed an obvious decrease from 7.5 to 2.9 ns after forming the composite. According to the literature, the lifetime of $CsPb(Br_xCl_{1-x})_3$ only changes slightly compared to $CsPbBr_3$;[52] thus, the decrease can be assigned to more effective electron extraction in the composite.[53]

The enhanced photocatalytic performance of the $CsPbX_3$/g-C_3N_4 composites can be attributed to several factors. First, the introduction of g-C_3N_4 endows the composite with a large surface area and an improved light-harvesting ability above 550 nm. Second, the heterojunction is believed to create transfer pathways for the photogenerated charge carriers. In our $CsPbX_3$/g-C_3N_4 composites, the valence band (VB) edges of pCN, $CsPbBr_3$, and 3Br−2CN were estimated to be 1.55, 0.82, and 1.38 eV, respectively, by executing XPS VB spectra (Figure S10b). Taking into account the band gaps, the CB edges of the above samples are −0.8, −1.45, and −1.08 eV. Thus, the CB of the as-obtained samples are more negative than the reduction potential level of CO_2/CO (−0.53 V *vs* NHE). As can be seen in Figure 6, under light irradiation, photoinduced electron and hole pairs are generated and tend to migrate. Typically, the holes from the VB of g-C_3N_4 would migrate to that of $CsPbBr_3$, where H_2O will be trapped to generate O_2 and protons. In parallel, the electrons from the CB of $CsPbBr_3$ will transfer to g-C_3N_4, where the activated CO_2 can be reduced to

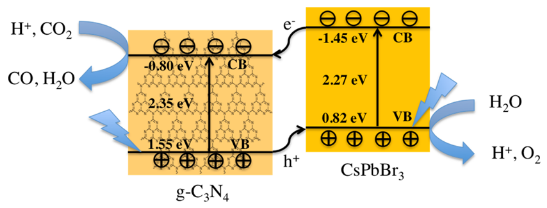

Figure 6. Schematic representation of the CO_2 photoreduction process on $CsPbX_3$/g-C_3N_4.

CO with the help of the generated protons. During the *in situ* growth of g-C_3N_4 in the presence of $CsPbBr_3$, a considerable amount of water could soak in and accumulate on the outer surface of g-C_3N_4, where the water oxidation reaction could also happen. The introduction of g-C_3N_4 not only helps to improve the stability and performance of $CsPbBr_3$ but also serves as an important photocatalyst itself. The synergetic catalytic effects play an important role in the photocatalytic reaction.[54]

3. CONCLUSIONS

We have successfully developed new $CsPbX_3$/g-C_3N_4 composites by a simple *in situ* solvothermal synthesis. The $CsPb(Br_xCl_{1-x})_3$ species exhibit an homogeneous dispersion in the heterostructures. The obtained $CsPbX_3$/g-C_3N_4 composites show a significantly improved CO_2 photoreduction activity, where 3Br−2CN has the highest CO produced rate, which is about five times of that on the pure constituents. The enhanced photoactivity is mainly attributed to the enlarged surface area, increased light-harvesting capability, the efficient separation of the photogenerated charge carriers caused by the perfect matching of the band structures, and the solid bonding interfaces between $CsPbBr_3$ and g-C_3N_4. This work shows that stability engineering of perovskites by constructing perovskite-based heterostructure photocatalysts is a promising route toward exploiting the outstanding perovskite semiconductor properties in efficient solar energy conversion. Furthermore, water is an important medium involved in most of the photocatalytic reactions; thus, the stability of perovskites in aqueous solution is critical if we want to make practical use of them in photocatalysis. As compared to pure perovskites, the generation of perovskite-based composites is a step forward toward creating water-stable photocatalysts. In this context, incorporating perovskites within an ultrathin layer of graphene, within a metal−organic framework or other porous hosts, or efficient packing and subsequent shielding between appropriate hole and electron transport layers could protect them from the environment and endow them with enhanced photocatalytic performance and stability for aqueous phase photocatalysis.

4. EXPERIMENTAL SECTION

4.1. Synthesis Photocatalysts. Pure $CsPbBr_3$ was synthesized following an anti-solvent method reported by Huang *et al.*[15] 2.5 mmol of cesium bromide (CsBr, Alfa Aesar, 99.9%) and 2 mmol of lead(II) bromide ($PbBr_2$, Aldrich, ≥98%) were dissolved in 15 mL of dimethyl sulphoxide (anhydrous, VWR Chemicals, ≥99.9%) and stirred for 12 h. The solution was quickly added into 150 mL of toluene under vigorous stirring. The obtained product was collected after centrifuging and washing by toluene. After drying in the vacuum oven at 80 °C, an orange-colored $CsPbBr_3$ powder was obtained.

Pure g-C_3N_4 was synthesized according to the literature.[30] In a typical procedure, 2 mmol of cyanuric chloride (TCI, >97%) and 1 mmol of melamine (Fluka Chemika, 99%) powders were put into a 100 mL Teflon-lined autoclave filled with 60 mL of acetonitrile (anhydrous, VWR Chemicals, 99.8%). The mixture was stirred for 24 h after which the autoclave was sealed and maintained at 180 °C for 12 h. The obtained product was washed with distilled water to remove residual impurities and then dried at 80 °C. The sample thus obtained was named as pCN.

As a reference sample, 20 g of urea (Aldrich, >99%) was placed into an alumina crucible with a cover and heated to 550 °C for 2 h at a heating rate of 5 °C min^{-1}.

For the $CsPbX_3$/gC_3N_4 composites, 2 mmol of cyanuric chloride and 1 mmol of melamine powders were added into 60 mL of acetonitrile and the mixture was stirred for 12 h. Then, 0.4, 0.3, 0.2, or 0.05 g (0.7, 0.5, 0.3, or 0.1 mmol) of $CsPbBr_3$ was added to the precursor solution, and it was stirred for another 12 h. The mixture was transferred to an autoclave and maintained at 180 °C for 12 h. The powder was washed with toluene and dried at 80 °C in the vacuum oven. In the composites, the $CsPbBr_3$ perovskite can contain a small amount of Cl, forming a $CsPb(Br_xCl_{1-x})_3$/gC_3N_4 composition, shortly $CsPbX_3$/gC_3N_4. For easy reading, the obtained samples will be further named as 2Br−CN, 3Br−2CN, Br−CN, and Br−4CN, respectively.

4.2. Characterization. XRD measurements were taken with a Stoe X-ray diffractometer using Cu Kα_1 radiation (λ = 1.5406 Å). SEM images of samples were performed on a FEI-Q FEG250 microscope, equipped with an EDAX system. XPS data were recorded on an ESCALAB 250 spectrometer with a monochromatized Al Kα_1 X-rays as the excitation source. All binding energies were corrected by fitting the C 1s peak of surface adventitious carbon at 284.8 eV. The optical absorption of the samples was studied using a Lambda-950 UV−vis spectrometer. The steady-state PL spectra were recorded on an Edinburgh FLS980, under an excitation wavelength of 380 nm. Nitrogen adsorption−desorption isotherms at 77 K were carried out on a Micromeritics 3Flex surface analyzer. Before the measurement, all the samples were degassed at 130 °C for 12 h under flowing N_2. TEM images were obtained on a CM200FEG PHILIPS operated at 200 kV, equipped with an EDAX system and a GATAN Tridiem Image Filter. TGA was performed from room temperature to 800 °C at a heating rate of 10 °C min^{-1} under O_2. Fluorescence lifetime data were acquired on a home-built confocal FLIM microscope based on a single photon counting (TCSPC) device (Picoquant). The pulse frequency of the 485 nm laser diode was set at 5 MHz, and the emission was filtered by a 530 ± 25 nm bandpass filter.

4.3. Photocatalytic CO_2 Reduction Measurement. Photocatalytic reduction of CO_2 was performed in a homemade Pyrex reactor (volume: 150 mL). A 300 W Xe lamp with a 420 cut-off filter (Newport) was used as the light source and positioned 5 cm away from the photocatalytic reactor. A test sample was prepared by uniformly dispersing a 20 mg photocatalyst toluene suspension on a thin glass plate with an area of 4 cm^2. The as-prepared sample plate was left in the vacuum oven at 80 °C for 18 h to eliminate the solvent. Before the reaction, high purity helium gas first flowed through the reactor for about 20 min to eliminate the air in the reactor. The test atmosphere was a mixture of CO_2 and water vapor, generated by passing high purity CO_2 (99.99%) gas through a

https://dx.doi.org/10.1021/acsomega.0c02960
ACS Omega 2020, 5, 24495−24503

water bubbler. After flowing the reactor for another 40 min with He, the measurement started under visible light (above 420 nm). After every 1 h of light irradiation, the evolved gas product was detected using a gas chromatograph (GC-2014, Shimadzu, Japan) with a thermal conductivity detector and a flame ionization detector, equipped with a ShinCarbon packed column. The carrier gas used in the GC-2014 was high purity helium. A typical GC chromatogram for the 3Br−2CN composite is depicted as Figure S6. After 24 h photostability measurement, the sample was collected and treated at 80 °C in the vacuum oven overnight.

■ ASSOCIATED CONTENT

Supporting Information

The Supporting Information is available free of charge at https://pubs.acs.org/doi/10.1021/acsomega.0c02960.

XRD pattern of $CsPbBr_3$ and 3Br−2CN before and after photocatalytic reaction, SEM images and mapping of 3Br−2CN, TGA thermograms, XPS spectra, GC chromatogram of 3Br−2CN, time-dependent CO generation, stability test, N_2 adsorption−desorption analysis, and Tauc plots (PDF)

■ AUTHOR INFORMATION

Corresponding Authors

Johan Hofkens − *Department of Chemistry, Faculty of Science, KU Leuven, 3001 Leuven, Belgium; Max Planck Institute for Polymer Research, 55128 Mainz, Germany;* orcid.org/0000-0002-9101-0567; Email: johan.hofkens@kuleuven.be

Elke Debroye − *Department of Chemistry, Faculty of Science, KU Leuven, 3001 Leuven, Belgium;* orcid.org/0000-0003-1087-4759; Email: elke.debroye@kuleuven.be

Authors

Ruolin Cheng − *Department of Chemistry, Faculty of Science, KU Leuven, 3001 Leuven, Belgium*

Handong Jin − *Department of Chemistry, Faculty of Science, KU Leuven, 3001 Leuven, Belgium*

Maarten B. J. Roeffaers − *Centre for Membrane Separations, Adsorption, Catalysis and Spectroscopy for Sustainable Solutions (cMACS), KU Leuven, 3001 Leuven, Belgium;* orcid.org/0000-0001-6582-6514

Complete contact information is available at: https://pubs.acs.org/10.1021/acsomega.0c02960

Author Contributions

R.C. and H.J. carried out the experimental work and analysis. R.C., M.B.J.R., J.H., and E.D. designed the concept and supervised the experiments. The manuscript was written through the contributions of all authors. All authors have given approval to the final version of the manuscript.

Notes

The authors declare no competing financial interest.

■ ACKNOWLEDGMENTS

The authors acknowledge financial support from the Research Foundation—Flanders (FWO) through a postdoctoral fellowship to E.D. (FWO grant no. 12O3719N) and research projects to J.H. and M.B.J.R (FWO grant nos. G098319N and ZW15_09-GOH6316), the European Union (Horizon 2020) Marie Sklodowska-Curie innovation program (grant no. 722591 and a Ph.D. fellowship to R.C.), the KU Leuven Research Fund (C14/15/053 and C14/19/079), and the Flemish government through long term structural funding Methusalem (CASAS2, Meth/15/04).

■ REFERENCES

(1) Fujishima, A.; Honda, K. Electrochemical Photolysis of Water at a Semiconductor Electrode. *Nature* **1972**, *238*, 37−38.

(2) Habisreutinger, S. N.; Schmidt-Mende, L.; Stolarczyk, J. K. Photocatalytic Reduction of CO_2 on TiO_2 and Other Semiconductors. *Angew. Chem., Int. Ed.* **2013**, *52*, 7372−7408.

(3) Indrakanti, V. P.; Kubicki, J. D.; Schobert, H. H. Photoinduced activation of CO_2 on Ti-based heterogeneous catalysts: Current state, chemical physics-based insights and outlook. *Energy Environ. Sci.* **2009**, *2*, 745−758.

(4) Tran, P. D.; Wong, L. H.; Barber, J.; Loo, J. S. C. Recent advances in hybrid photocatalysts for solar fuel production. *Energy Environ. Sci.* **2012**, *5*, 5902−5918.

(5) Zeng, S.; Kar, P.; Thakur, U. K.; Shankar, K. A review on photocatalytic CO_2 reduction using perovskite oxide nanomaterials. *Nanotechnology* **2018**, *29*, 052001−052022.

(6) Niu, G.; Guo, X.; Wang, L. Review of recent progress in chemical stability of perovskite solar cells. *J. Mater. Chem. A* **2015**, *3*, 8970−8980.

(7) Islam, M. J.; Shahjahan, M.; Yuyama, K.-i.; Biju, V. Remote Tuning of Bandgap and Emission of Lead Perovskites by Spatially Controlled Halide Exchange Reactions. *ACS Mater. Lett.* **2020**, *2*, 403−408.

(8) Huang, H.; Pradhan, B.; Hofkens, J.; Roeffaers, M. B. J.; Steele, J. A. Solar-Driven Metal Halide Perovskite Photocatalysis: Design, Stability, and Performance. *ACS Energy Lett.* **2020**, *5*, 1107−1123.

(9) Kang, B.; Biswas, K. Exploring Polaronic, Excitonic Structures and Luminescence in Cs_4PbBr_6/$CsPbBr_3$. *J. Phys. Chem. Lett.* **2018**, *9*, 830−836.

(10) Dana, J.; Maity, P.; Jana, B.; Maiti, S.; Ghosh, H. N. Concurrent Ultrafast Electron- and Hole-Transfer Dynamics in $CsPbBr_3$ Perovskite and Quantum Dots. *ACS Omega* **2018**, *3*, 2706−2714.

(11) Wu, H. L.; Li, X. B.; Tung, C. H.; Wu, L. Z. Semiconductor Quantum Dots: An Emerging Candidate for CO_2 Photoreduction. *Adv. Mater.* **2019**, *31*, 1900709−1900731.

(12) Chouhan, L.; Ghimire, S.; Subrahmanyam, C.; Miyasaka, T.; Biju, V. Synthesis, optoelectronic properties and applications of halide perovskites. *Chem. Soc. Rev.* **2020**, *49*, 2869−2885.

(13) Hou, J.; Cao, S.; Wu, Y.; Gao, Z.; Liang, F.; Sun, Y.; Lin, Z.; Sun, L. Inorganic Colloidal Perovskite Quantum Dots for Robust Solar CO_2 Reduction. *Chem.—Eur. J.* **2017**, *23*, 9481−9485.

(14) Xu, Y.-F.; Yang, M.-Z.; Chen, B.-X.; Wang, X.-D.; Chen, H.-Y.; Kuang, D.-B.; Su, C.-Y. A $CsPbBr_3$ Perovskite Quantum Dot/Graphene Oxide Composite for Photocatalytic CO_2 Reduction. *J. Am. Chem. Soc.* **2017**, *139*, 5660−5663.

(15) Huang, H.; Yuan, H.; Janssen, K. P. F.; Solís-Fernández, G.; Wang, Y.; Tan, C. Y. X.; Jonckheere, D.; Debroye, E.; Long, J.; Hendrix, J.; Hofkens, J.; Steele, J. A.; Roeffaers, M. B. J. Efficient and Selective Photocatalytic Oxidation of Benzylic Alcohols with Hybrid Organic-Inorganic Perovskite Materials. *ACS Energy Lett.* **2018**, *3*, 755−759.

(16) Ou, M.; Tu, W.; Yin, S.; Xing, W.; Wu, S.; Wang, H.; Wan, S.; Zhong, Q.; Xu, R. Amino-Assisted Anchoring of $CsPbBr_3$ Perovskite Quantum Dots on Porous g-C_3N_4 for Enhanced Photocatalytic CO_2 Reduction. *Angew. Chem., Int. Ed.* **2018**, *57*, 13570−13574.

(17) Pan, A.; Ma, X.; Huang, S.; Wu, Y.; Jia, M.; Shi, Y.; Liu, Y.; Wangyang, P.; He, L.; Liu, Y. $CsPbBr_3$ Perovskite Nanocrystal Grown on MXene Nanosheets for Enhanced Photoelectric Detection and Photocatalytic CO_2 Reduction. *J. Phys. Chem. Lett.* **2019**, *10*, 6590−6597.

(18) Wan, S.; Ou, M.; Zhong, Q.; Wang, X. Perovskite-type $CsPbBr_3$ quantum dots/UiO-66(NH_2) nanojunction as efficient visible-light-driven photocatalyst for CO_2 reduction. *Chem. Eng. J.* **2019**, *358*, 1287−1295.

https://dx.doi.org/10.1021/acsomega.0c02960
ACS Omega 2020, 5, 24495−24503

(19) Mollick, S.; Mandal, T. N.; Jana, A.; Fajal, S.; Desai, A. V.; Ghosh, S. K. Ultrastable Luminescent Hybrid Bromide Perovskite@ MOF Nanocomposites for the Degradation of Organic Pollutants in Water. *ACS Appl. Nano Mater.* **2019**, *2*, 1333−1340.

(20) Kong, Z.-C.; Liao, J.-F.; Dong, Y.-J.; Xu, Y.-F.; Chen, H.-Y.; Kuang, D.-B.; Su, C.-Y. Core@Shell $CsPbBr_3$@Zeolitic Imidazolate Framework Nanocomposite for Efficient Photocatalytic CO_2 Reduction. *ACS Energy Lett.* **2018**, *3*, 2656−2662.

(21) Huang, H.; Yuan, H.; Zhao, J.; Solís-Fernández, G.; Zhou, C.; Seo, J. W.; Hendrix, J.; Debroye, E.; Steele, J. A.; Hofkens, J.; Long, J.; Roeffaers, M. B. J. C(sp(3))-H Bond Activation by Perovskite Solar Photocatalyst Cell. *ACS Energy Lett.* **2019**, *4*, 203−208.

(22) Poli, I.; Hintermair, U.; Regue, M.; Kumar, S.; Sackville, E. V.; Baker, J.; Watson, T. M.; Eslava, S.; Cameron, P. J. Graphite-protected $CsPbBr_3$ perovskite photoanodes functionalised with water oxidation catalyst for oxygen evolution in water. *Nat. Commun.* **2019**, *10*, 2097.

(23) Yao, E. P.; Yang, Z. L.; Meng, L.; Sun, P. Y.; Dong, S. Q.; Yang, Y.; Yang, Y. High-Brightness Blue and White LEDs based on Inorganic Perovskite Nanocrystals and their Composites. *Adv. Mater.* **2017**, *29*, 1606859−1606865.

(24) Zhou, Z. Q.; Cui, Y.; Deng, H. X.; Huang, L.; Wei, Z. M.; Li, J. B. Modulation of electronic and optical properties in mixed halide perovskites $CsPbCl_{3x}Br_{3(1-x)}$ and $CsPbBr_{3x}I_{3(1-x)}$. *Appl. Phys. Lett.* **2017**, *110*, 113901−113905.

(25) Feng, X. B.; Ju, H. M.; Song, T. H.; Fang, T. S.; Liu, W. C.; Huang, W. Highly Efficient Photocatalytic Degradation Performance of $CsPb(Br_{1-x}Cl_x)(3)$-Au Nanoheterostructures. *ACS Sustainable Chem. Eng.* **2019**, *7*, 5152−5156.

(26) Chen, Y.; Jia, G.; Hu, Y. F.; Fan, G. Z.; Tsang, Y. H.; Li, Z. S.; Zou, Z. G. Two-dimensional nanomaterials for photocatalytic CO_2 reduction to solar fuels. *Sustainable Energy Fuels* **2017**, *1*, 1875−1898.

(27) Ou, M.; Tu, W.; Yin, S.; Xing, W.; Wu, S.; Wang, H.; Wan, S.; Zhong, Q.; Xu, R. Amino-Assisted Anchoring of $CsPbBr_3$ Perovskite Quantum Dots on Porous g-C_3 N_4 for Enhanced Photocatalytic CO_2 Reduction. *Angew. Chem., Int. Ed.* **2018**, *57*, 13570−13574.

(28) Zhao, Y.; Wang, Y.; Liang, X.; Shi, H.; Wang, C.; Fan, J.; Hu, X.; Liu, E. Enhanced photocatalytic activity of Ag-$CsPbBr_3$/CN composite for broad spectrum photocatalytic degradation of cephalosporin antibiotics 7-ACA. *Appl. Catal., B* **2019**, *247*, 57−69.

(29) You, S. Q.; Guo, S. H.; Zhao, X.; Sun, M.; Sun, C. Y.; Su, Z. M.; Wang, X. L. All-inorganic perovskite/graphitic carbon nitride composites for CO_2 photoreduction into C1 compounds under low concentrations of CO_2. *Dalton Trans.* **2019**, *48*, 14115−14121.

(30) Cui, Y. J.; Ding, Z. X.; Fu, X. Z.; Wang, X. C. Construction of Conjugated Carbon Nitride Nanoarchitectures in Solution at Low Temperatures for Photoredox Catalysis. *Angew. Chem., Int. Ed.* **2012**, *51*, 11814−11818.

(31) Chen, D. Q.; Fang, G. L.; Chen, X. Silica-Coated Mn-Doped CsPb(Cl/Br)(3) Inorganic Perovskite Quantum Dots: Exciton-to-Mn Energy Transfer and Blue-Excitable Solid-State Lighting. *ACS Appl. Mater. Interfaces* **2017**, *9*, 40477−40487.

(32) Cheng, R.; Zhang, L.; Fan, X.; Wang, M.; Li, M.; Shi, J. One-step construction of FeO_x modified g-C_3N_4 for largely enhanced visible-light photocatalytic hydrogen evolution. *Carbon* **2016**, *101*, 62−70.

(33) Kulbak, M.; Gupta, S.; Kedem, N.; Levine, I.; Bendikov, T.; Hodes, G.; Cahen, D. Cesium Enhances Long-Term Stability of Lead Bromide Perovskite-Based Solar Cells. *J. Phys. Chem. Lett.* **2016**, *7*, 167−172.

(34) Li, Z. J.; Hofman, E.; Li, J.; Davis, A. H.; Tung, C. H.; Wu, L. Z.; Zheng, W. W. Photoelectrochemically Active and Environmentally Stable $CsPbBr_3$/TiO(2)Core/Shell Nanocrystals. *Adv. Funct. Mater.* **2018**, *28*, 1704288−1704294.

(35) Wang, M.; Shen, M.; Zhang, L. X.; Tian, J. J.; Jin, X. X.; Zhou, Y. J.; Shi, J. L. 2D-2D MnO_2/g-C_3N_4 heterojunction photocatalyst: In-situ synthesis and enhanced CO_2 reduction activity. *Carbon* **2017**, *120*, 23−31.

(36) Liu, J. H.; Zhang, T. K.; Wang, Z. C.; Dawson, G.; Chen, W. Simple pyrolysis of urea into graphitic carbon nitride with recyclable adsorption and photocatalytic activity. *J. Mater. Chem.* **2011**, *21*, 14398−14401.

(37) Li, M.; Zhang, L.; Fan, X.; Wu, M.; Wang, M.; Cheng, R.; Zhang, L.; Yao, H.; Shi, J. Core-shell $LaPO_4$/g-C_3N_4 nanowires for highly active and selective CO_2 reduction. *Appl. Catal., B* **2017**, *201*, 629−635.

(38) Ravi, V. K.; Santra, P. K.; Joshi, N.; Chugh, J.; Singh, S. K.; Rensmo, H.; Ghosh, P.; Nag, A. Origin of the Substitution Mechanism for the Binding of Organic Ligands on the Surface of $CsPbBr_3$ Perovskite Nanocubes. *J. Phys. Chem. Lett.* **2017**, *8*, 4988−4994.

(39) Pal, P.; Saha, S.; Banik, A.; Sarkar, A.; Biswas, K. All-Solid-State Mechanochemical Synthesis and Post-Synthetic Transformation of Inorganic Perovskite-type Halides. *Chem.—Eur. J.* **2018**, *24*, 1811−1815.

(40) Xia, J. X.; Di, J.; Li, H. T.; Xu, H.; Li, H. M.; Guo, S. J. Ionic liquid-induced strategy for carbon quantum dots/BiOX (X=Br, Cl) hybrid nanosheets with superior visible light-driven photocatalysis. *Appl. Catal., B* **2016**, *181*, 260−269.

(41) Jain, D.; Mamtani, K.; Gustin, V.; Gunduz, S.; Celik, G.; Waluyo, I.; Hunt, A.; Co, A. C.; Ozkan, U. S. Enhancement in Oxygen Reduction Reaction Activity of Nitrogen-Doped Carbon Nanostructures in Acidic Media through Chloride-Ion Exposure. *ChemElectroChem* **2018**, *5*, 1966−1975.

(42) Liu, C.; Zhang, Y.; Dong, F.; Reshak, A. H.; Ye, L.; Pinna, N.; Zeng, C.; Zhang, T.; Huang, H. Chlorine intercalation in graphitic carbon nitride for efficient photocatalysis. *Appl. Catal., B* **2017**, *203*, 465−474.

(43) Zhao, Y. L.; Wei, Y. C.; Wu, X. X.; Zheng, H. L.; Zhao, Z.; Liu, J.; Li, J. M. Graphene-wrapped Pt/TiO_2 photocatalysts with enhanced photogenerated charges separation and reactant adsorption for high selective photoreduction of CO_2 to CH_4. *Appl. Catal., B* **2018**, *226*, 360−372.

(44) Pu, Y.-C.; Fan, H.-C.; Liu, T.-W.; Chen, J.-W. Methylamine lead bromide perovskite/protonated graphitic carbon nitride nanocomposites: interfacial charge carrier dynamics and photocatalysis. *J. Mater. Chem. A* **2017**, *5*, 25438−25449.

(45) Li, M.; Zhang, L.; Wu, M.; Du, Y.; Fan, X.; Wang, M.; Zhang, L.; Kong, Q.; Shi, J. Mesostructured CeO_2/g-C_3N_4 nanocomposites: Remarkably enhanced photocatalytic activity for CO_2 reduction by mutual component activations. *Nano Energy* **2016**, *19*, 145−155.

(46) Liu, L. J.; Gao, F.; Zhao, H. L.; Li, Y. Tailoring Cu valence and oxygen vacancy in Cu/TiO_2 catalysts for enhanced CO_2 photoreduction efficiency. *Appl. Catal., B* **2013**, *134*, 349−358.

(47) Akbali, B.; Topcu, G.; Guner, T.; Ozcan, M.; Demir, M. M.; Sahin, H. $CsPbBr_3$ perovskites: Theoretical and experimental investigation on water-assisted transition from nanowire formation to degradation. *Phys. Rev. Mater.* **2018**, *2*, 034601−034607.

(48) Manser, J. S.; Christians, J. A.; Kamat, P. V. Intriguing Optoelectronic Properties of Metal Halide Perovskites. *Chem. Rev.* **2016**, *116*, 12956−13008.

(49) Rao, L. S.; Tang, Y.; Yan, C. M.; Li, J. S.; Zhong, G. S.; Tang, K. R.; Yu, B. H.; Li, Z. T.; Zhang, J. Z. Tuning the emission spectrum of highly stable cesium lead halide perovskite nanocrystals through poly(lactic acid)-assisted anion-exchange reactions. *J. Mater. Chem. C* **2018**, *6*, 5375−5383.

(50) Han, Q. J.; Wu, W. Z.; Liu, W. L.; Yang, Q. X.; Yang, Y. Q. Temperature-dependent photoluminescence of $CsPbX_3$ nanocrystal films. *J. Lumin.* **2018**, *198*, 350−356.

(51) Ravi, V. K.; Markad, G. B.; Nag, A. Band Edge Energies and Excitonic Transition Probabilities of Colloidal $CsPbX_3$ (X = Cl, Br, I) Perovskite Nanocrystals. *ACS Energy Lett.* **2016**, *1*, 665−671.

(52) Chen, H.; Guo, A.; Gu, X.; Feng, M. Highly luminescent $CsPbX_3$ (X=Cl, Br, I) perovskite nanocrystals with tunable photoluminescence properties. *J. Alloys Compd.* **2019**, *789*, 392−399.

(53) Zhan, X.; Jin, Z.; Zhan, J.; Bai, D.; Bian, H.; Wang, K.; Sun, J.; Wang, Q.; Liu, S. F. All-Ambient Processed Binary $CsPbBr_3$-$CsPb_2Br_5$ Perovskites with Synergistic Enhancement for High-Efficiency Cs-Pb-

Br-Based Solar Cells. *ACS Appl. Mater. Interfaces* **2018**, *10*, 7145−7154.
(54) Shi, J. L. On the Synergetic Catalytic Effect in Heterogeneous Nanocomposite Catalysts. *Chem. Rev.* **2013**, *113*, 2139−2181.

NOTE ADDED AFTER ASAP PUBLICATION

Figure 1 was incorrect in the version that published on September 16, 2020; the correct version reposted on September 17, 2020.

https://dx.doi.org/10.1021/acsomega.0c02960
ACS Omega 2020, 5, 24495−24503